PERGAMON

International Journal of Heat and Mass Transfer 44 (2001) 3529–3541

International Journal of HEAT and MASS TRANSFER

www.elsevier.com/locate/ijhmt

Heat transfer and pressure drop in a rectangular channel with diamond-shaped elements

Giovanni Tanda *

Dipartimento di Termoenergetica e Condizionamento Ambientale, Università degli Studi di Genova, via all'Opera Pia 15/a, I-16145 Genova, Italy

Received 13 April 2000; received in revised form 16 October 2000

Abstract

Heat transfer and pressure drop experiments were performed for a rectangular channel equipped with arrays of diamond-shaped elements. Both in-line and staggered fin arrays were considered, for values of the longitudinal and transverse spacings, relative to the diamond side, from 4 to 8 and from 4 to 8.5, respectively. The height-to-side ratio of the diamonds was 4.0. Liquid crystal thermography was used to determine the heat transfer coefficients on the surface of the channel (endwall) on which the fins were mounted. Local variations in heat transfer coefficients induced by the arrangements of the diamond-shaped elements were measured and discussed. Correlations giving the average Nusselt number for each fin configuration as a function of the Reynolds number were developed. Thermal performance comparisons with data for a rectangular channel without fins showed that the presence of the diamond-shaped elements enhanced heat transfer by a factor of up to 4.4 for equal mass flow rate and by a factor of up to 1.65 for equal pumping power.

1. Introduction

Heat transfer associated with flow over arrays of pin fins has been the subject of extensive investigation in the past because of its importance in a wide variety of engineering applications, such as compact heat exchangers and the cooling of advanced gas turbine blades and electronic devices. A pin-fin array usually consists of a number of cylinders attached perpendicularly to the bounding duct walls (endwalls), with the coolant fluid passing crossflow over the cylinders. Much of the literature published is devoted to the study of the flow normal to banks of circular cylinders [1–8]. When the cylinder height-to-diameter ratio is very large (higher than 4) the fin geometry is of particular interest in heat exchanger applications, in which the attainment of very high heat transfer coefficients is of major concern. The heat transfer rates at the endwalls, and the endwall effects on the fin surface heat transfer adjacent to the walls, are unimportant. Arrays of pin fins with low/intermediate height-to-diameter ratio (from 0.5 to 4) are commonly used in internally cooled gas turbine engine airfoils. Here the pins must be relatively short because of passage size and manufacturing limitations; as a consequence, cylinder/endwall interactions are strong and the analysis of the overall thermal performance must include heat transfer from the endwall surface. Indeed, the heat transfer coefficients of short pins, which are significantly lower than those of long fins, are typically comparable to those at the endwall.

Sparrow et al. [1,2] were among the first to investigate the heat transfer performance of in-line and staggered wall-attached arrays of cylindrical fins. The longitudinal and transverse spacing-to-diameter ratios were kept fixed and equal to 3 and 2.6, respectively, while the fin height varied from 29% to 87.5% of the channel height. The performance comparison between the two different fin arrangements showed that the in-line array provided a higher heat transfer rate than that from the staggered array by a factor of up to 1.2 under conditions of equal pumping power and equal heat transfer area. On the other hand, at a fixed heat duty and fixed mass flow rate,

* Tel.: +390-10-353-2881; fax: +390-10-311-870.
E-mail address: tanda@ditec.unige.it (G. Tanda).

0017-9310/01/$ - see front matter
PII: S0017-9310(01)00018-7

Nomenclature

A	heat transfer surface area
A_{ch}	flow area of the channel without fins
A_{min}	minimum cross-sectional area
D_{ch}	hydraulic diameter of the channel without fins
f	apparent friction factor
f_0	friction factor for the channel without fins
K_p	per-row pressure coefficient
k	thermal conductivity of air
H	height of the diamond-shaped elements
h	heat transfer coefficient
L	heat transfer surface length
$\dot{m}$	mass flow rate
N	number of rows in a diamond-shaped array
Nu	Nusselt number based on the hydraulic diameter D_{ch} $(= hD_{ch}/k)$
Nu_{av}	average Nusselt number based on the hydraulic diameter D_{ch}
Nu^*_{av}	average Nusselt number based on the diamond side W $(= Nu_{av}(W/D_{ch}))$
Nu_0	fully developed Nusselt number for the asymmetrically heated, unfinned channel
P	pressure
Pr	Prandtl number
Re	Reynolds number of the channel, $\dot{m}D_{ch}/(\mu A_{ch})$
Re^*	Reynolds number based on the diamond side and the minimum flow area, $\dot{m}W/(\mu A_{min})$
Re_0	Reynolds number of the asymmetrically heated, unfinned channel
Q_{dis}	heat transfer rate dissipated by thermal conduction
Q_{el}	power input
Q_{fins}	heat transfer rate from fins
Q_{rad}	heat transfer rate dissipated by thermal radiation
q_{conv}	convective heat flux
S_L	spacing of the diamond-shaped elements in the longitudinal direction
S_T	spacing of the diamond-shaped elements in the transverse direction
$T_{air,x}$	bulk temperature of air at x-position
T_{LC}	surface temperature detected by liquid crystals
x	longitudinal coordinate
W	side of the diamond-shaped element
w	mean air velocity in the channel, $\dot{m}/(\rho A_{ch})$
w_{max}	mean air velocity in the minimum flow area A_{min}, $\dot{m}/(\rho A_{ch})$

Greek symbols

Δ	difference
μ	dynamic viscosity of air
ρ	density of air

the staggered array required a 14% shorter heat transfer surface than the in-line array.

Local and average heat transfer from staggered arrays of pin fins was extensively studied by Metzger et al. [3,4]. Experimental results for short fins (height-to-diameter ratio of 1) and for various longitudinal and transverse pin spacings were presented. It was found that more closely spaced fins performed better for the same temperature driving potential, with differences in Nusselt numbers between the most closely spaced array (spacing-to-diameter ratio of 1.05) and the most widely spaced array (dimensionless spacing equal to 5) from 50% to 100%, depending on the value of the Reynolds number [3]. For moderate dimensionless streamwise spacings (from 1.5 to 2.5), local heat transfer was seen to increase in the streamwise direction for the first several rows until a peak was reached at about the third to fifth row; heat transfer then decreased slightly in the streamwise direction [4]. This last finding was confirmed by Simoneau and VanFossen [5], who performed an experimental study of heat transfer from a staggered array of pin fins with dimensionless longitudinal and transverse spacings of 2.67; the recorded turbulence intensity profiles along the streamwise coordinate exhibited similar features to the local heat transfer results.

Further studies focused on typical aspects of turbine cooling applications, such as the effects of the presence of a rounded junction between the pin and the endwall [6] and of short or long ejection holes deployed laterally along the pin fin channel [7]. The endwall heat transfer in the presence of in-line and staggered adiabatic pin fins was studied by Matsumoto et al. [8]. The endwall heat transfer coefficients obtained for the staggered arrays were slightly higher than those recorded for the in-line arrays with the same height and spacing. Relative to endwalls without pins, heat transfer was enhanced by a factor of 2.3–2.9, depending on the Reynolds number.

While the literature regarding circular cylinders is abundant, only few data exist for arrays of diamond-shaped pin fins. A diamond element is essentially a square prism rotated 45° relative to the direction of the mainstream flow. Grannis and Sparrow [9,10] performed experiments and numerical simulations for two diamond-shaped fin geometries; attention was focused on pressure drop and fluid flow characteristics, and heat transfer was not considered. Heat transfer modifications induced by a single diamond-shaped element mounted on a flat baseplate were studied in [11]. More recently, Chyu et al. [12] investigated the heat transfer performance of arrays of cubic and diamond-shaped fins inside a rectangular channel; only two arrangements of

diamond-shaped fins were considered (staggered and in-line) and endwall heat transfer was not analysed. Tanda et al. [13,14] experimentally investigated heat transfer characteristics for diamond-shaped fin arrays with different degrees of fin populations. Fins were made integral with the baseplate, so both fin surface and endwall surface were thermally active. Local (per-module) and average heat transfer coefficients were determined and a relationship between dimensionless groups was presented.

The present work was performed to analyse heat transfer and pressure drop in a rectangular channel equipped with arrays of diamond-shaped pin fins. The diamond-shaped elements were not heated and, owing to their low thermal conductivity, were considered to be adiabatic for the thermal boundary condition. Therefore, attention was focused on local and average heat transfer coefficients on the heated endwall plate. The airflow was bounded by the heated endwall and by three unheated plates to form a rectangular channel whose height was equal to the fin height. Both the population and the arrangement (staggered or in-line) of the diamond elements were varied. Experimental results were also compared with data for a rectangular channel without fins, in order to evaluate the degree of heat transfer enhancement induced by the diamond-shaped elements both for the constant mass flow rate and constant pumping power constraints.

2. Experimental apparatus and procedure

2.1. Experimental setup

The description of the experimental apparatus is facilitated by reference to Fig. 1. Main components are: the wind tunnel, the test section, the heating arrangement and the instrumentation. An open-circuit suction-type wind tunnel was used for this study. Air, drawn at room temperature, passed through a filter and entered a rectangular channel (0.1 m wide and 0.02 m high, hydraulic diameter $D_{ch} = 0.033$ m) in which the test section was fitted. The rectangular channel consisted of a hydrodynamic development section, the test section, and the exit section. This duct was followed by a long circular channel containing a control valve to set the mass flow rate and a Venturi flowmeter to measure it, and terminated at the blower inlet. The air discharged from the blower was ducted out of the laboratory room.

The test section was a rectangular channel, as wide and high as the entry and exit sections and delimited by a thin heated plate (0.1 m wide and 0.28 m long) and

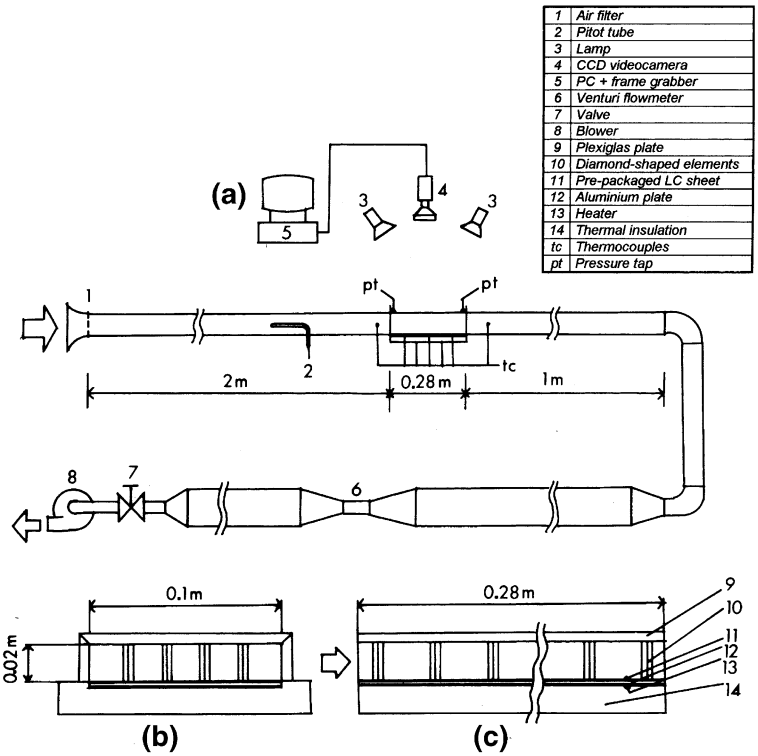

Fig. 1. Experimental apparatus: (a) schematic diagram; (b), (c) test section details.

lateral and frontal Plexiglas walls. The plate was made of 0.5 mm aluminium sheet to which a plane heater had been attached to provide a controllable uniform heat flux. On the side opposed to the heater, a thin liquid crystal (LC) sheet was applied in order to measure local wall temperature.

The side walls of the test section were covered by thermal insulation layers in order to convoy to the convective air flow as much as possible of the electric power dissipated by the heater. Power was supplied by an adjustable DC source and measured by a voltmeter and an amperometer. Fine-gauge thermocouples were placed inside the rectangular channel directly exposed to the airflow and in several places inside the channel wall material. These sensors were used to measure the air temperature at the test section inlet, to estimate conduction heat losses to the surroundings and to control the attainment of the steady-state conditions. Pressure taps, connected to a common alcohol manometer, were located at the inlet and outlet of the test section in the streamwise direction. A Pitot tube probe located in the development section (sufficiently far from the inlet of the test section) was used for the additional measurement of mass flow rate.

Thermosensitive, cholesteric LCs were used to measure the temperature distributions on the heated surface. The pre-packaged LC sheet (0.15 mm thick) consisted of a thermochromic LC layer (on a black background) applied onto a mylar film and backed with a pressure-sensitive adhesive. The colour distribution of the LCs was observed by a CCD video camera through the Plexiglas wall opposite to the heated surface and stored in a PC equipped with a frame grabber. Four 100-W lamps were used to illuminate the test section during image storing. The lamps were switched on only for the time strictly required for image acquisition, in order to avoid radiant heating of the test surface.

Diamond-shaped elements were made of Plexiglas and glued onto the heated plate. Owing to their low thermal conductivity, the diamond elements were considered to be adiabatic and their function was to generate turbulence in the airflow in order to increase the endwall heat transfer. The elements were arranged in staggered and in-line arrays, at various longitudinal and transverse spacing distances.

2.2. Fin geometry

The diamond-shaped elements (side $W = 0.5$ cm, height $H = 2$ cm, height-to-side ratio $= 4$) were installed over the heated plate in various array patterns. Typical patterns of staggered and in-line arrays of diamond-shaped fins are shown in Fig. 2, in which transverse and longitudinal spacings, respectively denoted by S_T and S_L, are also indicated. Geometric parameters of fin arrays are summarised in Table 1. Fin configurations A and B are arranged in-line and present different degrees of fin populations; in particular, the relative transverse and longitudinal spacings for configuration A are double those for configuration B. Fin arrays C–F have a staggered arrangement; configurations C–D–E have approximately the same transverse spacing (40–42.4 mm) while the longitudinal spacing varies from 40 to 21.2 mm. Configuration F presents a dense arrangement of diamonds spaced 20 mm apart along transverse and longitudinal directions. As emerges from inspection of the table, the performance of configurations A and C can be directly compared with each other (S_T and S_L are the same), as can configurations B and F. Comparison of performance of configurations C–D–E enables the effect of the longitudinal spacing S_L (for the staggered arrangement) to be discerned.

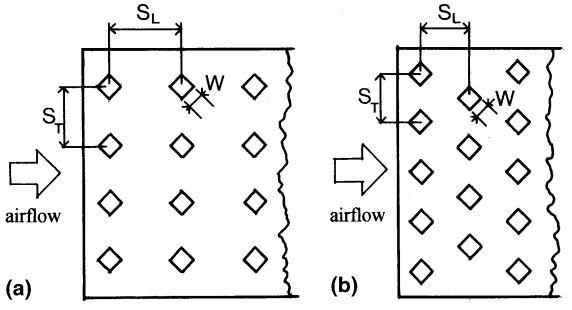

Fig. 2. Arrangements of diamond-shaped elements: (a) in-line; (b) staggered.

Table 1
Configuration of the arrays investigated

Configuration	Arrangement	No. fins per row	No. rows	No. fins	S_T (mm)	S_L (mm)	S_T/W	S_L/W
A	In-line	2	7	14	40	40	8	8
B	In-line	4	13	52	20	20	4	4
C	Staggered	Sequences of 2–3	7	18	40	40	8	8
D	Staggered	Sequences of 2–3	10	25	40	30	8	6
E	Staggered	Sequences of 2–3	14	35	42.4	21.2	8.5	4.2
F	Staggered	Sequences of 4–5	13	59	20	20	4	4

2.3. Calibration of thermosensitive liquid crystals

The relationship between the colour and temperature of the thermosensitive LCs was found by calibration experiment. The calibration test was carried out by gradually heating a 5 mm thick aluminium plate (calibration plate) covered by a LC film identical to that used in the experiments. The calibration plate was placed in the test section and equipped with 10 fine-gauge type-K thermocouples calibrated to ±0.1 K. The thermocouples, housed in small holes drilled in the material at different positions as closed to the surface as possible, were used to measure the wall temperature and the degree of surface temperature uniformity. The inlet and outlet passages of the test section were blocked during the calibration test in order to promote isothermal conditions inside the test section. For a given wall temperature, the corresponding colour image displayed by the LCs was digitised and processed in order to obtain, pixel by pixel, the hue, saturation, intensity (HSI) contents from the red, green, blue (RGB) domain. Among the new parameters (HSI) only hue was retained since it was found to be the only one correlated with the surface temperature [15]. The hue–temperature correlation of calibration data is reported in Fig. 3 and depends not only on the type of LCs but also on the recording angle, and on the features of the illumination and of the test section (presence of transparent or reflecting walls). The hue–temperature correlation was found to be fairly linear and repeatable in the range from 30.5°C to 32.5°C, corresponding to the range of hue (expressed on an eight-bit integer scale) between 42.5 and 142.5. Regression of data turned out to be particularly accurate in the 70–130 hue range: this field of hue was therefore selected for the quantitative analysis of each LC image. The corresponding calibration line has an uncertainty band (at the 95% confidence interval) of ±0.2 K. In order to minimise the hysteresis phenomena detected by Baughn et al. [16], care was taken to avoid reaching very high temperatures (say higher than 40°C) on the test surface in relation to the LC working temperature.

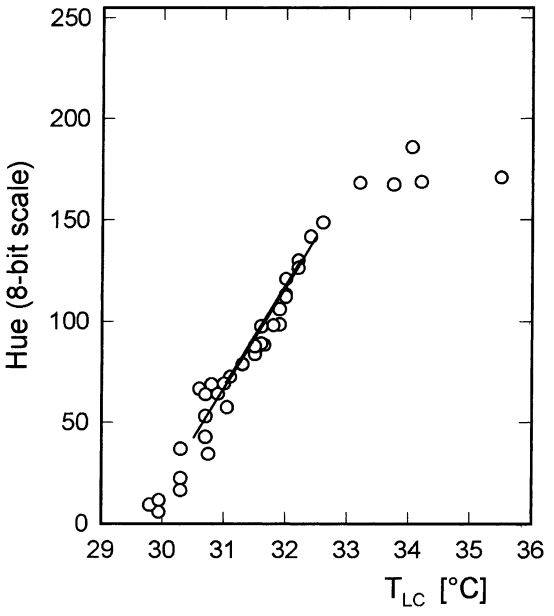

Fig. 3. Hue–temperature calibration with regression line.

2.4. Operating procedure and data reduction

After the fin array had been set and the airflow had been adjusted to a prescribed velocity, the DC current was supplied to the heater. The surface temperature was maintained within the thermosensitivity region of the LCs by controlling the input power delivered to the heater. Once steady-state conditions were reached, input power, thermocouple readings and the LC images were recorded; these data were then processed in order to extract the local heat transfer coefficient according to the following relationship:

$$h = q_{\mathrm{conv}}/(T_{\mathrm{LC}} - T_{\mathrm{air},x}), \tag{1}$$

where q_{conv} is the convective heat flux, assumed to be uniformly distributed over the heated plate, T_{LC} is the surface temperature detected by the LCs and $T_{\mathrm{air},x}$ is the bulk temperature of the air at the x position along the streamwise direction. $T_{\mathrm{air},x}$ was determined by measuring the air temperature at the entrance of the test section (where the flow is isothermal) and assuming a linear rise along the test duct. The convective heat flux was evaluated as follows:

$$q_{\mathrm{conv}} = (Q_{\mathrm{el}} - Q_{\mathrm{rad}} - Q_{\mathrm{dis}} - Q_{\mathrm{fins}})/A, \tag{2}$$

where Q_{el} is the measured input power to the heater, Q_{rad} is the calculated radiative heat transfer rate to the surroundings, Q_{dis} is the calculated heat transfer rate dissipated through the insulation on the rear face of the heater and A is the area of the plate surface exposed to the airflow. The term Q_{fins} takes into account the heat dissipation from the diamond fins. Even though the diamonds were deemed to be adiabatic owing to their low thermal conductance, the conventional one-dimensional fin model was applied to estimate the small amount of heat transfer rate delivered to the airflow from their sides. If the heat transfer coefficient along the fin is assumed to be equal to the average heat transfer coefficient over the baseplate, Q_{fins}, calculated by an iterative procedure, is always less than 5% of Q_{el}, namely $Q_{\mathrm{fins}}/Q_{\mathrm{el}}$ is approximately equal to the ratio between the baseplate surface area occupied by the fins and the total area (0.1 m × 0.28 m) of the baseplate. The sum of Q_{rad} and Q_{dis} was always found to be within 6–10% of Q_{el}. The convective heat flux q_{conv} varied from about 300 to 2000 W/m^2 depending on the test conditions; the cor-

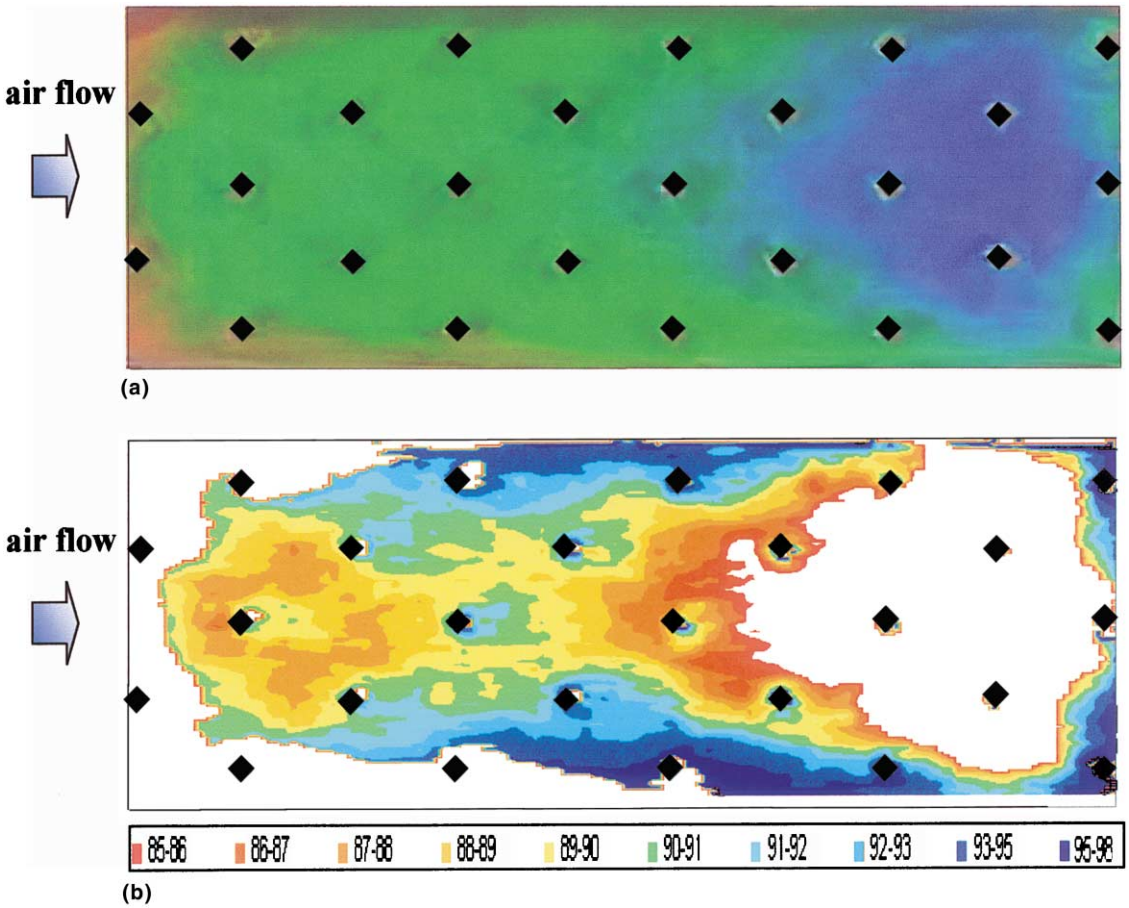

Fig. 4. Example of LC image capture and processing: (a) map of displayed colours; (b) corresponding map of heat transfer coefficient (SI units).

responding range of variation of the electrical (input) flux was about 350–2300 W/m^2. Air temperature rises along the test section were typically within 2 K in the presence of average plate-to-air temperature differences of about 8–12 K.

Local and average heat transfer coefficients were recast in terms of Nusselt number, defined as follows:

$$Nu = hD_{ch}/k. \tag{3}$$

The Reynolds number was defined as

$$Re = \dot{m}D_{ch}/(\mu A_{ch}), \tag{4}$$

where $\dot{m}$ is the mass flow rate, A_{ch} is the flow area offered by the rectangular channel without fins, and D_{ch} is the hydraulic diameter of the rectangular channel. Thermal conductivity k and dynamic viscosity μ of air were evaluated at the film temperature.

To obtain a dimensionless representation of the pressure drop due to the fin array, a per-row, dimensionless, pressure coefficient K_p was introduced:

$$K_p = (\Delta P/N)/(\rho w_{max}^2/2), \tag{5}$$

where ΔP is the difference between static pressures recorded at the pressure taps that immediately preceded and followed the fin array, N is the number of fin rows, ρ is the air density just upstream of the array and w_{max} is the air velocity defined as:

$$w_{max} = \dot{m}/(\rho A_{min}), \tag{6}$$

A_{min} being the minimum cross-sectional area. For the purpose of comparison with the hydraulic performance of the channel without fins, an apparent friction factor f was evaluated from the following equation:

$$f = (\Delta P/L)D_{ch}/(\rho w^2/2), \tag{7}$$

where L is the axial distance between the two pressure taps and w is the mean velocity in the channel given by:

$$w = \dot{m}/(\rho A_{ch}). \tag{8}$$

Both the pressure coefficient and the apparent friction factor are based on adiabatic conditions (i.e., test without heating).

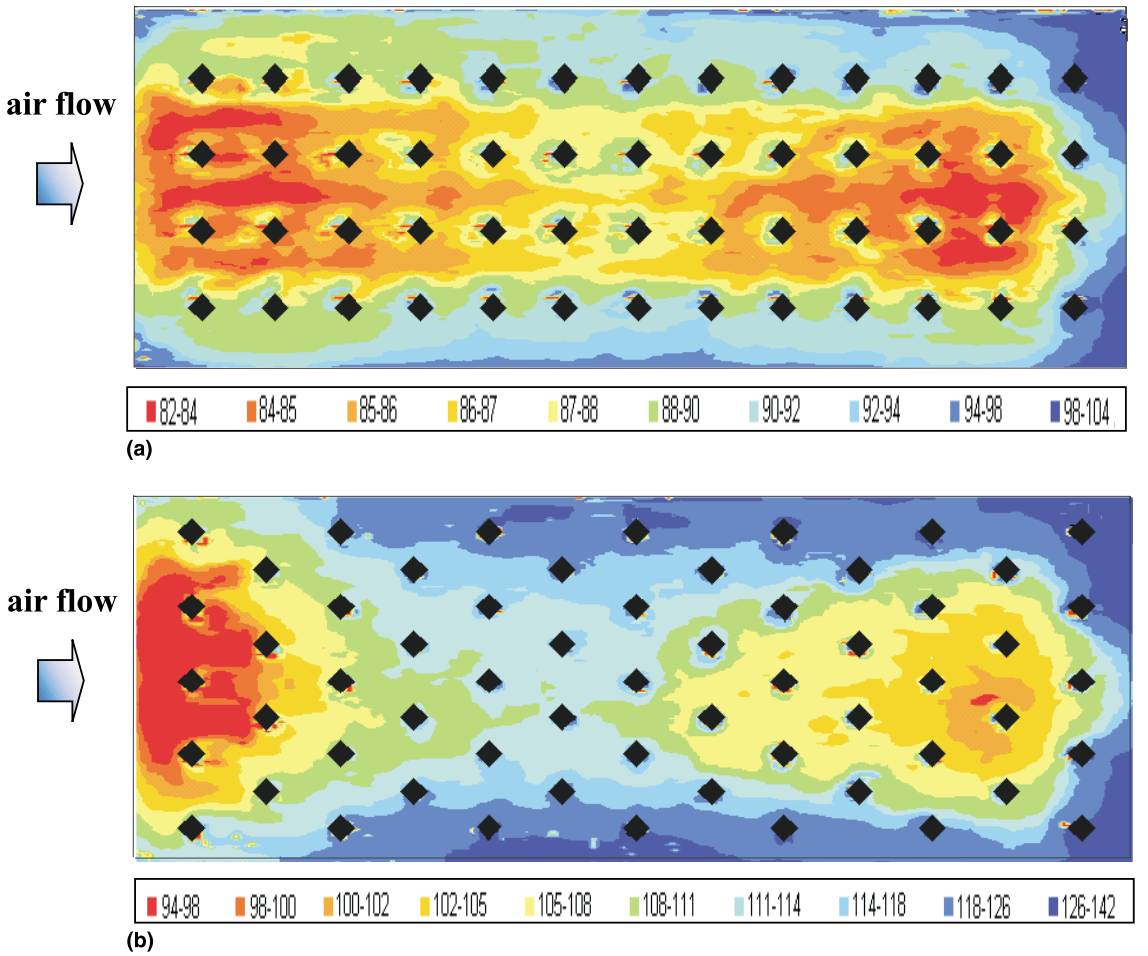

Fig. 5. Maps of heat transfer coefficients (in W/m^2 K) at $Re = 15\,800$: (a) configuration B; (b) configuration F.

2.5. The image processing system

The image of the coloured pattern of LCs was taken by the CCD video camera and converted by the frame grabber to a BMP file, for subsequent manipulation by standard graphical packages and by the algorithm for the RGB to HSI pixel-by-pixel conversion. A convolution filter was used to minimise the effects of image defects producing, in isolated pixels, values of hue not correlated to the surface temperature. The final step consisted of applying custom-made software to convert the hue into the surface temperature and to evaluate the local heat transfer coefficient via Eq. (1).

Once the steady state for a test at a given air flow rate and input power had been reached, the LC image was taken by the video camera. An example of such an image is reported in Fig. 4(a). From the LC image, the local heat transfer coefficient was reconstructed over the region of the heated plate matched by LCs when local temperature was within the working temperature interval. Even though colours are exhibited over the whole surface, only points having the hue within the 70–130 range have been processed: the corresponding values of the heat transfer coefficient are plotted in Fig. 4(b). It is apparent from the figure that the heat transfer coefficient is not obtained over the entire surface. Outside the selected hue interval, no information is gained; therefore, in those cases, tests were repeated at the same air flow rate and for 2–3 different values of the input power (typically varying the input power by $\pm 20\%$), this in order to "shift" the colour pattern toward the regions not previously monitored and to locally extract the values of the heat transfer coefficient via Eq. (1).

2.6. Experimental uncertainties

Uncertainty analysis was performed by applying the estimation method proposed by Moffat [17]. The uncertainty estimation (at the 95% confidence level) of the heat transfer coefficient must take into account several

sources of error: measuring system errors in Q_{el} (voltage and current readings), T_{air} (thermocouple readings) and T_{LC} (liquid–crystal thermographic reading), conceptual errors in q_{conv} (mainly ascribed to the effect of axial thermal conduction along the aluminium plate), processing system errors associated with the procedure adopted to treat the LC images, and variable errors associated with the lack of repeatability caused by random disturbances and unsteadiness. When only the measuring system errors and variable errors are considered, the uncertainty in local h values is estimated to be $\pm 4.8\%$. This value rises to $\pm 6.5\%$ when errors due to axial conduction and to the processing of the LC images are taken into account. The Reynolds number has a calculated uncertainty of $\pm 3.2\%$. Finally, the uncertainty in the pressure drop coefficients (K_p and f) was estimated to be $\pm 7.8\%$ at the lowest Reynolds numbers and $\pm 3.4\%$ at the highest Reynolds numbers.

3. Results and discussion

3.1. Local heat transfer coefficients

Diamond fins are expected to induce high levels of the heat transfer coefficient at the endwall. This is mainly due to the vortex generation at the fin-endwall junctions. The wake shedding generated by each fin interacts with those promoted by adjacent fins and with the fin placed immediately behind, giving rise to a complex pattern of flow which greatly affects the heat transfer characteristics. Examples of heat transfer coefficient maps are shown in Fig. 5; experimental data, obtained at a given Reynolds number ($Re = 15800$), are plotted for the in-line configuration B in Fig. 5(a) and for the staggered configuration F in Fig. 5(b). A glance at these figures reveals excellent data symmetry, which attests to the quality of the present experiment.

Of particular interest are the distributions of the heat transfer coefficient along the normalised longitudinal coordinate x/L (L being the heated surface length) recorded along columns of fins or between adjacent columns. These distributions are reported, for two different Reynolds numbers (8800 and 20 000), in Figs. 6 and 7 for both the in-line configurations and in Figs. 8–10 for three of the staggered configurations. Each figure reports the sketch of the array indicating any individual trajectory along which h is presented. Distributions along lines intersecting sequences of fins do not include points up to 1 mm immediately downstream and/or upstream of the fin-endwall junction, to which optical access was not feasible.

3.1.1. In-line configurations

For configuration A (Fig. 6), the heat transfer coefficient distribution along line I (intersecting the centres

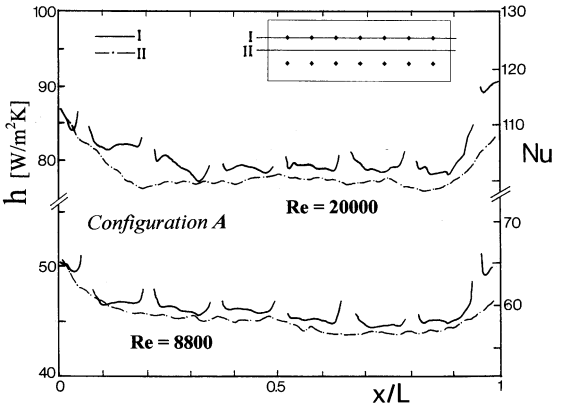

Fig. 6. Distributions of the heat transfer coefficient along the normalised streamwise coordinate for the in-line configuration A, at $Re = 8800$ and 20 000.

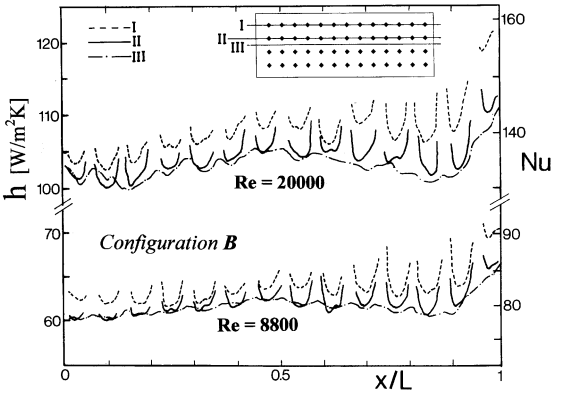

Fig. 7. Distributions of the heat transfer coefficient along the normalised streamwise coordinate for the in-line configuration B, at $Re = 8800$ and 20 000.

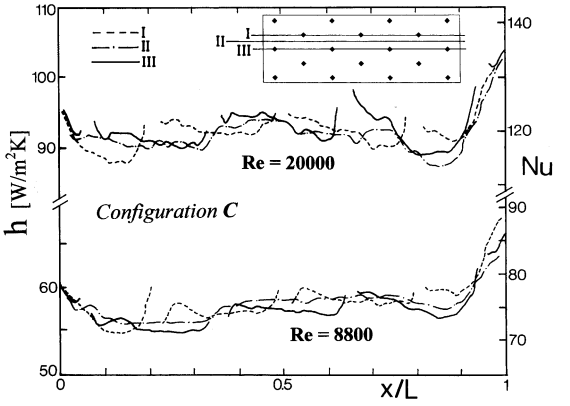

Fig. 8. Distributions of the heat transfer coefficient along the normalised streamwise coordinate for the staggered configuration C, at $Re = 8800$ and 20 000.

of diamonds) is characterised by high values immediately upstream (owing to the impinging effect) and downstream (owing to the vortex generation) of each diamond-shaped element. One or more relative maxima appear between two successive diamonds; this effect, related to the wake characteristics induced by each pin fin, is more noticeable for the larger Reynolds number, when the turbulence level is higher. The inter-fin h profiles recorded downstream of the first two rows of fins are almost repetitive in shape, denoting the attainment of periodic, fully developed conditions. Distributions along line II refer to the longitudinal symmetry line of the plate: here, the heat transfer coefficient first decreases with the longitudinal coordinate and then reaches a quasi-constant value. The further lift-off in h values upstream of the exit, found for all the fin configurations, may be associated with extraneous conduction losses along the wall material. As compared with distribution along line I, profiles along line II present slightly lower h values, for both the Reynolds numbers, probably owing to the reduced lateral spreading of wakes induced by this array configuration.

As the fin population is increased (configuration B, Fig. 7), h profiles along the centre-to-centre lines (I and II) typically exhibit a U-shape between successive fins, with strong reductions from the fin-endwall junction to the middle of the inter-fin spacing. Edge effects are responsible for differences between the distributions along lines I and II spaced by the S_T distance along the transverse direction. Values of h recorded along line III (which is the longitudinal symmetry line of the fin array) have relative maxima at the sections of reduced flow area. Heat transfer coefficients measured at periodically positioned stations tend to increase slightly up to about the fifth-sixth row of elements owing to the increasing levels of turbulence intensity. Downstream, a gradual decay is observed up to the vicinity of the exit section, where end effects are present.

3.1.2. Staggered configurations

Fig. 8 shows the heat transfer coefficient distributions for configuration C, in which the diamond-shaped elements are staggered and widely spaced. Inspection of the figure reveals that the h profiles along the inter-fin segments (lines I and III) are very similar to each other, taking into account the shifting by S_L along the streamwise coordinate x. At the lower Reynolds number, the maximum inter-fin values in h are generally reached 10–20 mm downstream of the fin-endwall junction (probably the location of flow reattachment) rather than immediately downstream of the junction; this is in agreement with results reported in the literature [11] for the single diamond element. At the higher Reynolds number, the reattachment-induced enhancements in h values are comparable to or less than those occurring just downstream of the junction itself. Moreover, the

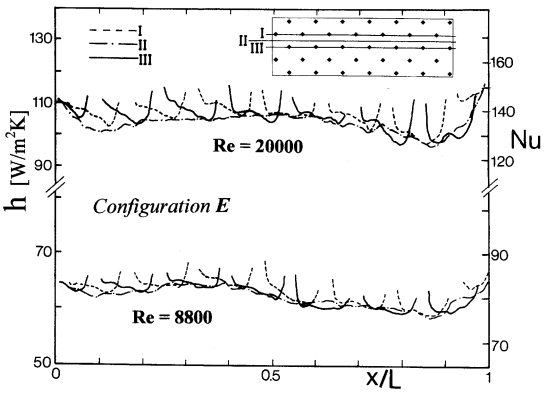

Fig. 9. Distributions of the heat transfer coefficient along the normalised streamwise coordinate for the staggered configuration E, at $Re = 8800$ and 20 000.

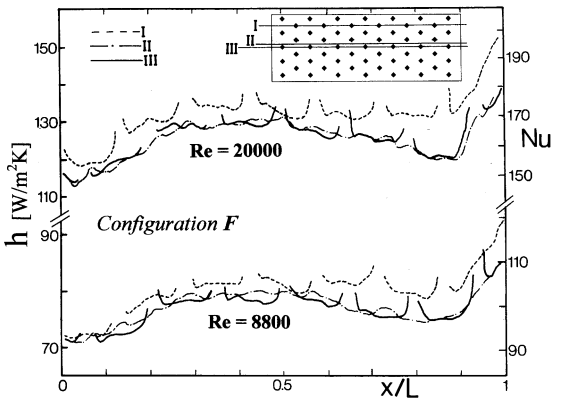

Fig. 10. Distributions of the heat transfer coefficient along the normalised streamwise coordinate for the staggered configuration F, at $Re = 8800$ and 20 000.

local heat transfer coefficient tends to decrease along the second half of the inter-fin segment, where the effect of the wake shedding is tempered. A further sudden increase in h is then recovered just upstream of the successive fin as a result of the flow impingement. For both the Reynolds number values, the values of the heat transfer coefficient along line II intermediate to two fin columns are comparable to those along the inter-fin segments: this means that the wakes generated by the staggered arrangement spread more widely (in the transverse direction) than those in the in-line arrangement.

As the longitudinal spacing S_L is reduced from 40 mm (configuration C) to 21.2 mm (configuration E, Fig. 9), the transverse spacing S_T being kept nearly constant (40–42.4 mm), the relative maxima along the inter-fin segments (lines I and III) are markedly retrenched or in practice disappear. Again, the local heat transfer

coefficients between adjacent columns of fins (lines II) are very close to those recorded in the inter-fin regions, thus indicating significant sideways wake-shedding.

Finally, configuration F, which is the densest staggered arrangement, shows the highest heat transfer coefficients, as emerges from inspection of Fig. 10. The inter-fin distributions (lines I and III) evidentiate the edge effects in the spanwise direction (line I is very close to the lateral boundary of the channel, while line III is symmetrical with the channel sides). The h-distributions recorded far from the lateral edges (namely along the central, inter-fin line III and the line II lying between two adjacent columns of fins) show a common behaviour. Aside from the increase towards the exit section, both the distributions of the heat transfer coefficient attain the highest values after 5–6 rows of elements (as found for the in-line configuration B) where the turbulence intensity becomes large; a noticeable reduction is then observed in the second half of the endwall surface.

3.2. Average heat transfer coefficients

To develop heat transfer correlations, the average heat transfer coefficients are required. The average Nusselt number was calculated by averaging the local Nu values within a surface area excluding the regions between the lateral columns of fins and the side walls and the regions, of length S_L, containing the first and the last fin rows. This in order to minimise the effects of the edge, inlet and outlet effects on the average heat transfer coefficient. Thus calculated, the average Nusselt number is typically 0–3% lower than that computed by considering the entire test surface.

Whereas the Nusselt and Reynolds numbers defined on the basis of the hydraulic diameter of the unfinned channel are useful for the purpose of comparison with the performance of the surface without fins, the following different definitions of the dimensionless groups were considered for the practical design:

$$Nu^* = hW/k, \tag{9}$$

$$Re^* = \dot{m}W/(\mu A_{\min}), \tag{10}$$

where the diamond side W is used as characteristic length in the Nusselt number Nu^* and the Reynolds number Re^* is based on the diamond side W, the mass flow rate $\dot{m}$ and the minimum cross-sectional area $A_{\min}$.

Figs. 11(a) and (b) show the area-averaged Nusselt number, for all the in-line and the staggered configurations, against the Reynolds number according to the different definitions of the dimensionless groups. The two area-averaged Nusselt numbers and the two Reynolds numbers are related by the following relationships:

$$Nu^*_{av} = Nu_{av}(W/D_{ch}), \tag{11}$$

$$Re^* = Re(W/D_{ch})(A_{ch}/A_{\min}). \tag{12}$$

The average Nusselt numbers Nu_{av} and Nu^*_{av} were represented by least-square curves fitting in the form of

$$Nu_{av} = aRe^b, \tag{13}$$

$$Nu^*_{av} = a^*(Re^*)^b, \tag{14}$$

where the coefficients a and a^* and the exponent b are listed in Table 2. The exponent b of the Reynolds number is in the 0.589–0.651 range for all the configurations and is lower than that obtained in [8] for endwalls with arrays of staggered ($b = 0.625$–0.698) and

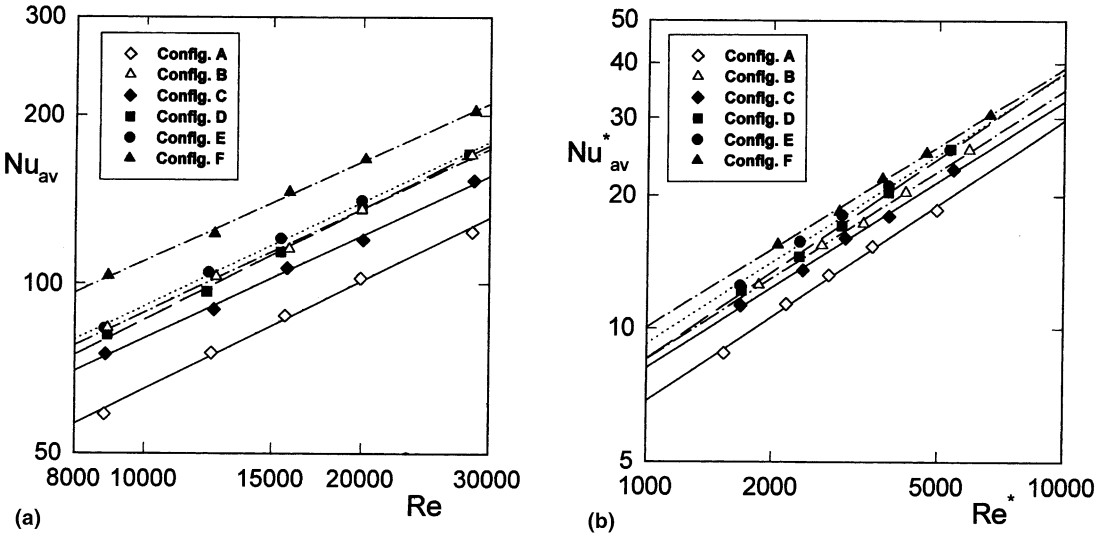

Fig. 11. Average Nusselt numbers for all the in-line and staggered configurations: (a) Nu_{av} versus Re; (b) Nu^*_{av} versus Re^*.

Table 2
Correlation coefficients for heat transfer relationships and pressure drop coefficients

Configuration	$Nu_{av} = aRe^b$, $Nu^*_{av} = a^*(Re^*)^b$			$\overline{K}_p$	$\overline{f}$
	a	a^*	b		
A (in-line)	0.184	0.084	0.637	0.144	0.046
B (in-line)	0.323	0.125	0.610	0.182	0.155
C (staggered)	0.302	0.124	0.606	0.252	0.093
D (staggered)	0.214	0.094	0.651	0.223	0.109
E (staggered)	0.318	0.133	0.615	0.212	0.142
F (staggered)	0.483	0.172	0.589	0.356	0.358

in-line ($b = 0.695$–0.750) cylindrical elements. This difference is attributable to the different characteristics of wakes induced by the diamond elements, as emphasised in [11,12].

An overall inspection of Figs. 11(a) and (b) reveals that the average Nusselt number of the staggered configurations is always higher than that of the in-line configurations that have the same transverse and longitudinal spacing. It is worth noting that, as the longitudinal spacing S_L of the staggered configuration is reduced from 40 to 30 mm and then from 30 to 21.2 mm, the transverse spacing S_T being kept approximately the same (40–42.4 mm), the average Nusselt numbers progressively increase, except for the highest Reynolds numbers, for which the heat transfer coefficients are only slightly affected by the reduction of S_L from 30 to 21.2 mm. The highest average Nusselt numbers are achieved by the staggered configuration *F*, which has the smallest values of the transverse and longitudinal spacings.

3.3. Pressure drop

Heat transfer enhancement is generally accompanied by a pressure penalty. Table 2 reports the values of the pressure coefficient K_p and the apparent friction factor f, respectively. Since these values showed only slight variations (always within $\pm 5\%$) with the Reynolds number, Reynolds-averaged coefficients have been presented for each configuration. As expected, pressure drop penalties are higher for the staggered configurations than for the in-line configurations with the same spacing parameters. Among the staggered configurations, the apparent friction factor f increases with the fin population, while the per-row pressure coefficient K_p is minimum for configuration E, despite the fairly large number of diamond-shaped elements.

3.4. Heat transfer performance comparison

Several performance comparison criteria for heat exchangers have been proposed in the literature (see for instance [18–20]). Bergles and Blumenkrantz [18] have suggested that the heat transfer from the enhanced surface (the endwall with fins) can be compared with that from a reference surface (the endwall without fins) according to given geometric and/or operating constraints. For instance the heat transfer augmentation provided by the enhanced geometry can be evaluated by keeping the mass flow rate constant or, alternatively, fixing the power required to pump the fluid (over the enhanced and reference surfaces).

For the purpose of comparison, the following relationships giving Nu_0 and f_0 for the fully developed turbulent flow in a rectangular channel (without fins and with asymmetric heating), have been considered:

$$Nu_0 = 0.019 Re_0^{0.8} Pr^{0.5}, \tag{15}$$

$$f_0 = 0.079 Re_0^{-0.25}, \tag{16}$$

where Re_0 is the Reynolds number based on the mass flow rate passing through the unfinned reference channel.

Comparison of the heat transfer performance under the same mass flow rate implies that the Reynolds numbers Re and Re_0 for the finned and the unfinned channels are equal to each other. The degree of heat transfer enhancement (relative to the unfinned surface), expressed by the ratio between Nu_{av} and Nu_0, is plotted in Fig. 12. As found by other Authors in similar studies [8,12], Nu_{av}/Nu_0 tends to decrease as the Reynolds number increases. The highest values of Nu_{av}/Nu_0, which were obtained for configuration *F*, are in the 3.4–4.4 range.

The quantity Nu_{av}/Nu_0 can be estimated according to the equal pumping-power performance criterion. In order to respect this constraint, the mass flow rates passing through the enhanced and reference channel cannot be the same; the assumption of constant pumping power leads to the following expression for the Reynolds numbers:

$$Re_0 = (f/f_0)^{1/3} Re = 2.517 f^{0.364} Re^{1.09}, \tag{17}$$

where Re_0 is the value of the Reynolds number to be used in Eq. (15) to evaluate Nu_0. The value of Nu_{av}/Nu_0 reported in Fig. 13 can determine whether or not a given surface is potentially advantageous under the

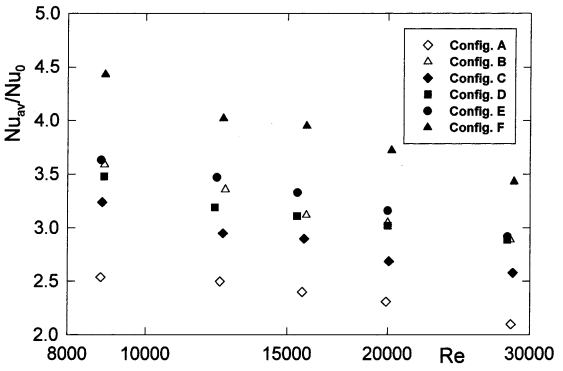

Fig. 12. Ratio of average Nusselt numbers with and without fins against the Reynolds number for fixed mass flow rates.

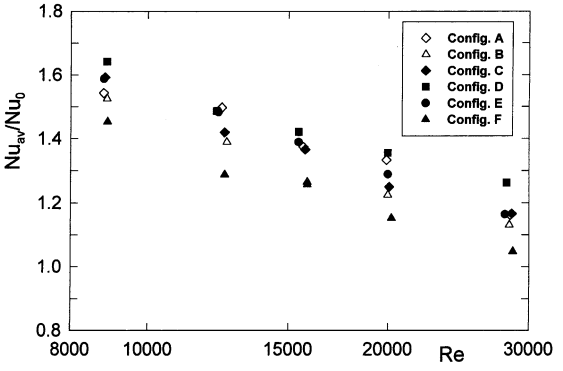

Fig. 13. Ratio of average Nusselt numbers with and without fins against the Reynolds number for fixed pumping powers.

requirement that the pumping power must be the same. According to the results shown in the figure, the degree of the heat transfer enhancement (here in the 1.05–1.65 range) is lower than that obtained for the fixed mass flow rate constraint. Thermal performance is generally improved when the fins are in-line rather than staggered with the same longitudinal and transverse spacings; the opposite conclusion has been reached previously for the comparison, presented in Fig. 12, without taking into account the pressure drop. The densest in-line and staggered configurations (B and F, respectively) are characterised by the lowest heat transfer augmentation (relative to the unfinned surface) among the geometries studied; therefore, when the pumping power requirements are taken into account, the use of closely spaced diamond-shaped elements appears to be of little value.

4. Conclusions

Forced convection in a rectangular channel with diamond-shaped elements has been experimentally investigated. The diamond-shaped elements were mounted on a surface of the channel (endwall) in order to analyse the modifications induced in the heat transfer characteristics, which were measured by means of LC thermography. Both in-line and staggered arrangements of the diamonds were considered, for different values of dimensionless longitudinal and transverse spacings ($S_L/W = 4$–8, $S_T/W = 4$–8.5) yielding a total of six configurations of diamond-shaped elements. The Reynolds number, based on the hydraulic diameter of the unfinned channel, was varied from 8000 to 30 000. The principal conclusions are the following:

(1) The distributions of the heat transfer coefficient h turned out to be strongly influenced, in their shape and level, by the geometric parameters of the diamond-shaped arrays. When fins are widely spaced, the inter-fin h values tend to reach, after the first one or two rows of elements, a periodically, fully developed distribution with period equal to S_L (in-line arrangements) or $2S_L$ (staggered arrangements); for closely spaced diamond configurations, h values still exhibit periodic variations with x/L, but, on an average, increase up to the fifth or sixth row of elements and then decrease slightly up to the exit section, where a sudden increase due to end effects is noticeable.

(2) The average Nusselt numbers have been expressed by power-law correlations versus the Reynolds number and comparatively examined; the exponent of the Reynolds number was found to be in the 0.59–0.65 range. Conversely, the pressure drop coefficients turned out to be insensitive to the Reynolds number.

(3) Heat transfer performance of the fin configurations has been discussed by considering the unfinned surface as a reference. When comparison is made for the same mass flow rate passing through the finned and unfinned channels, the staggered arrangements of diamonds closely spaced on the heat transfer surface gives the largest enhancement (from 3.4 to 4.4) in comparison with the unfinned surface. At equal pumping power, the best relative thermal performance (up to 1.65) is achieved by in-line and staggered arrangements with low-intermediate degrees of fin populations.

References

[1] E.M. Sparrow, J.W. Ramsey, Heat transfer and pressure drop for a staggered wall-attached array of cylinders with tip clearance, Int. J. Heat Mass Transfer 21 (1978) 1369–1377.

[2] E.M. Sparrow, J.W. Ramsey, C.A.C. Altemani, Experiments on in-line pin fin arrays and performance comparison with staggered arrays, ASME J. Heat Transfer 102 (1980) 44–50.

[3] D.E. Metzger, Z.X. Fan, W.B. Shepard, Pressure loss and heat transfer through multiple rows of short pin fins, in:

Proceedings of the Seventh Heat Transfer Conference, vol. 3, Hemisphere, Washington, DC, 1982, pp. 137–142.
[4] D.E. Metzger, R.A. Berry, J.P. Bronson, Developing heat transfer in rectangular ducts with staggered arrays of short pin fins, ASME J. Heat Transfer 104 (1982) 700–706.
[5] R.J. Simoneau, G.J. VanFossen, Effect of location in an array on heat transfer to a short cylinder in crossflow, ASME J. Heat Transfer 106 (1984) 42–48.
[6] M.K. Chyu, Heat transfer and pressure drop for short pin-fin arrays with pin-endwall fillet, ASME J. Heat Transfer 112 (1990) 926–932.
[7] T.K. Kumaran, J.C. Han, S.C. Lau, Augmented heat transfer in a pin fin channel with short or long ejection holes, Int. J. Heat Mass Transfer 34 (1991) 2617–2628.
[8] R. Matsumoto, S. Kikkawa, M. Senda, Effect of pin fin arrangement on endwall heat transfer, JSME Int. J., Series B 40 (1997) 142–151.
[9] E.M. Sparrow, V.B. Grannis, Pressure drop characteristics of heat exchangers consisting of arrays of diamond-shaped pin fins, Int. J. Heat Mass Transfer 34 (1991) 589–600.
[10] V.B. Grannis, E.M. Sparrow, Numerical simulation of fluid flow through an array of diamond-shaped pin fins, Numer. Heat Transfer, Part A 19 (1991) 381–403.
[11] M.K. Chyu, V. Natarajan, Heat transfer on the base surface of three-dimensional protruding elements, Int. J. Heat Mass Transfer 39 (1996) 2925–2935.
[12] M.K. Chyu, Y.C. Hsing, V. Natarajan, Convective heat transfer of cubic fin arrays in a narrow channel, ASME J. Turbomach. 120 (1998) 362–367.
[13] G. Tanda, C. Schenone, Perdite di carico e scambio termico in convezione forzata per schiere di alette prismatiche, in: Proceedings of the Ninth National (U.I.T.) Heat Transfer Conference, Pisa, Italy, 1991, pp. 525–539 (in Italian).
[14] G. Tanda, A. Massardo, C. Schenone, Studio sperimentale dello scambio termico convettivo in un canale rettangolare in presenza di alette prismatiche sfalsate, in: Proceedings of the 17th National (U.I.T.) Heat Transfer Conference, Ferrara, Italy, vol. I, 1999, pp. 15–26 (in Italian).
[15] C. Camci, K. Kim, S.A. Hippensteele, A new hue capturing technique for the quantitative interpretation of liquid crystal images used in convective heat transfer studies, ASME J. Turbomach. 114 (1992) 765–775.
[16] J.W. Baughn, M.R. Anderson, J.E. Mayhew, J.D. Wolf, Hysteresis of thermochromic liquid crystal temperature measurement based on hue, ASME J. Heat Transfer 121 (1999) 1067–1072.
[17] R.J. Moffat, Describing the uncertainties in experimental results, Exp. Thermal Fluid Sci. 1 (1988) 3–17.
[18] A.E. Bergles, A.R. Blumenkrantz, J. Taborek, Performance evaluation criteria for selection of enhanced heat transfer surfaces, in: Proceedings of the Fifth Heat Transfer Conference, The Japan Society of Mechanical Engineering, vol. 2, 1974, pp. 239–243.
[19] R.K. Shah, Compact heat exchanger surface selection methods, in: Proceedings of the Sixth Heat Transfer Conference, vol 4, Hemisphere, Washington DC, 1978, pp. 193–199.
[20] L. Tagliafico, G. Tanda, A thermodynamic method for the comparison of plate-fin heat exchanger performance, ASME J. Heat Transfer 118 (1996) 805–809.